Chemical Engineering Journal 102 (2004) 61–69

Chemical Engineering Journal

www.elsevier.com/locate/cej

Electrochemical model of the integrated planar solid oxide fuel cell (IP-SOFC)

Paola Costamagna [a,*], Azra Selimovic [b], Marco Del Borghi [a], Gerry Agnew [c]

[a] *DICHEP, University of Genoa, Via Opera Pia 15, 16145 Genoa, Italy*
[b] *Department of Heat and Power Engineering, Lund University, PO Box 118, S-221 00 Lund, Sweden*
[c] *Rolls-Royce Fuel Cell Systems Ltd, PO Box 31, Derby DE24 8BJ, UK*

Received 18 August 2003; accepted 22 February 2004

Abstract

The Integrated Planar Solid Oxide Fuel Cell (IP-SOFC) is an innovative fuel cell concept which is substantially a cross between tubular and planar geometries, seeking to borrow thermal compliance properties from the former and low cost component fabrication and short current paths from the latter. In this study, a simulation model for the IP-SOFC is presented, with particular highlight on the simulation of the local reaction, taking into account the chemical and electrochemical processes occurring at the electrodes, together with mass transport issues. Some aspects of the overall reactor simulation are discussed as well. The model results have been compared to the experimental data obtained from both a small scale IP-SOFC module and a full-size prototype; in both cases the agreement is good. This electrochemical model is the basis of a detailed model of the full-scale IP-SOFC reactor to be included into a plant simulation tool designed to support thermodynamic analysis of hybrid IP-SOFC/GT (Gas Turbine) systems.

Keywords: Fuel cells; Electrochemical reactors; Transport phenomena; Modelling

1. Introduction

Solid Oxide Fuel Cells (SOFC) have attracted considerable interest during the past decade as highly effective and environmentally acceptable sources of electrical energy. Among fuel cells, it is believed that they can offer a wide potential range of application and high system efficiency. They also have the potential to make use of waste heat released at high temperature in cogeneration applications and bottoming cycles. However, problems related to the mechanical stability of the materials involved and high fabrication costs arise, which have given incentive for the evaluation of several different cell geometries. The state-of-the-art geometries can be classified as planar/monolithic (a monolith being originated by a number of planar cells stacked together) [1] and tubular [2,3]. The former geometry has good features from the electrical point of view, due to short current paths within the cell resulting in low internal electrical resistances and consequently high power density. However, the main drawback of this design is that it is a monolithic structure built from brittle ceramic components with rather high thermal expansion coefficients. At the high SOFC operating temperature (about 1000 °C) the intrinsic lack of thermal expansion compliance can result in crackings of the solid structure, with consequent cross-over of reactants and loss of performance. On the other hand, tubular SOFCs are less mechanically constrained with regard to expansion and contraction, but from the electrical point of view they have rather long current paths, leading to high cell resistance. In order to avoid an increase of the length of the current paths over a certain value, the cell diameter must be kept small (about 2 cm) which is one of the reasons for the high manufacturing costs. Against this background, the integrated planar solid oxide fuel cell (IP-SOFC) is a new concept, which is substantially a cross between tubular and planar geometries, seeking to borrow thermal compliance qualities from the former and low cost component fabrication and short current paths from the latter [4]. A scheme of the IP-SOFC concept is reported in Fig. 1, where the chemical and electrochemical reactions are shown along with the current paths through each cell. Fig. 1a represents a section of each fuel cell, which clearly shows the sequence of the various components; the thickness of the electrodes and the electrolyte is about 20–30 μm each. In the IP-SOFC concept, several cells of small dimensions are deposited over a vertical porous substrate and

* Corresponding author. Tel.: +39-0103532922; fax: +39-0103532586.
E-mail address: paola.costamagna@unige.it (P. Costamagna).

1385-8947/$ – see front matter © 2004 Elsevier B.V. All rights reserved.
doi:10.1016/j.cej.2004.02.005

Nomenclature

b	thickness of gas flow duct (m)
B	parameter defined in Eq. (9) (–)
C	cross-plane resistance area ($\Omega\,m^2$)
D_{eff}	effective diffusion coefficient ($m^2\,s^{-1}$)
E	ohmic symmetry factor
F	Faraday constant ($C\,mol^{-1}$)
G	Gibbs free energy ($J\,mol^{-1}$)
i	current density (A/m^2)
i_0	exchange current density (A/m^2)
J	non-dimensional strip width
L	characteristic length (m)
n_e	number of exchanged electrons (–)
p	partial pressure (bar)
P	total pressure (bar)
r	reaction rate ($mol\,m^3\,s^{-1}$)
R	specific electrical resistance ($\Omega\,m^2$)
R_g	universal gas constant ($J\,mol^{-1}\,K^{-1}$)
t	thickness (m)
T	temperature (K)
V	voltage (V)
W	molar flow ($mol\,m^2\,s^{-1}$)
x	co-ordinate (m)
X	cell pitch length
y	molar fraction ($mol\,mol^{-1}$)

Greek symbols

α	charge transfer coefficient (–)
γ	pre-exponential factor (Eqs. (13)–(14)) (–)
η	voltage loss (V)
ν	stoichiometric coefficient (–)
ρ	resistivity ($\Omega\,m$)
σ	conductivity ($\Omega^{-1}\,m^{-1}$)

Subscripts

a	anode
act	activation
c	cathode
cca	current collector of the anode
ccc	current collector of the cathode
conc	concentration
i	component of PEN structure or of gas
ohm	ohmic

Superscripts

o	bulk flow
shift	shifting reaction
$*$	at the reaction site

electrically connected in series, in order to obtain high voltages and low electrical currents. Fig. 1b shows a front view of the *multi-cell module*, where the cells appear as small stripes. The module is fed externally with air and internally with fuel (through channels located inside the support).

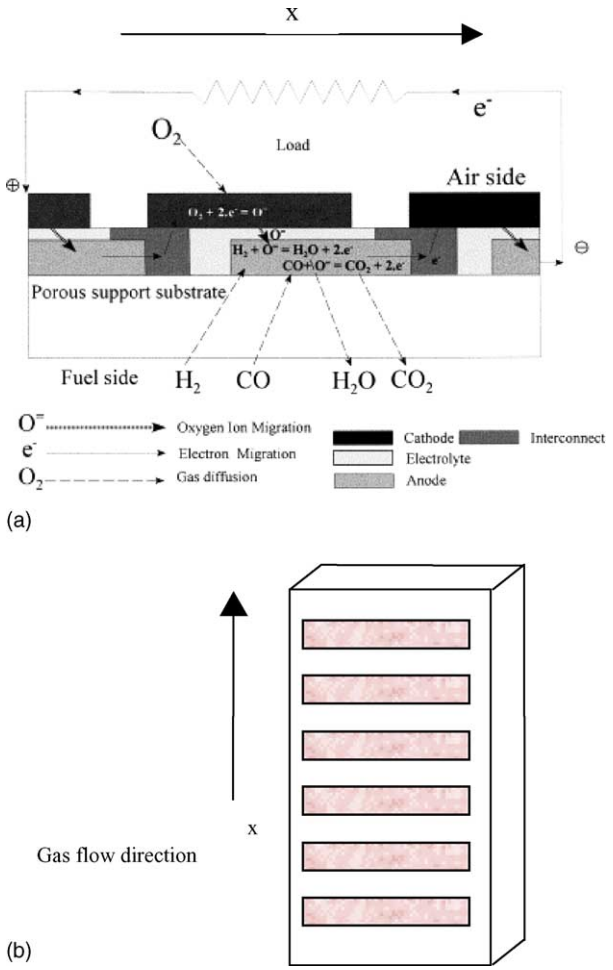

Fig. 1. (a) Schematic illustration of the multi-cell MEA concept; (b) module configuration.

The IP-SOFC stack is an essential part of a hybrid plant, which combines this technology together with a gas turbine in order to provide a high efficiency power generation system. Such systems are the focus of current research within a project supported by the European Union (more details are reported in the section 'Acknowledgements'). The goal of the present study was to develop and validate a suitable model of the local kinetics of the IP-SOFC, which could be the basis of a complete model of the IP-SOFC full-size reactor; the complete model could then be integrated in a system simulation tool designed to support thermodynamic analysis of hybrid IP-SOFC/GT systems.

2. Description of the experimental apparatus

The experimental apparatuses have been designed, built and operated by Rolls-Royce. The first tests concentrated on 3-cell modules, and thereafter scaling-up to 20-cell modules was achieved.

2.1. 3-Cell module

Electrochemical testing was carried out on samples with three cells screen printed on 50 mm × 50 mm porous calcia stabilised zirconia or magnesium aluminate substrates. In order to run the experimental tests, the sample was kept in a sample holder, where a stream of fuel was caused to flow over the inward facing support substrate and anodes, and a stream of air over the outward facing cathodes. In order to avoid any possibility of contact between fuel and air, the perimeter of the sample was sealed into the sample holder. Since the cells in the module were connected in series, they supplied the same electrical current at different operating voltages. The total effective electrode area of the sample was 13.44 cm^2 (3 cm × 4.48 cm). The sample was tested under different electrical loads using humidified H_2 (+3% H_2O) as fuel and air as oxidant at low reactant utilisations. Current–voltage (*I–V*) curves were measured at atmospheric pressure and over the temperature range of 689–989 °C, obtained by changing the temperature of the furnace where the samples, together with the sample holder, were placed.

2.2. 20-Cell module

Having achieved an adequate performance at the 3-cell level, scale-up of the multi-cell module was commenced [4]. The module was double-sided by depositing an identical series of multi-cells on both sides of a porous support (Fig. 1b). Each side consisted of 20, 0.8 cm × 5.6 cm, single cells which had total effective electrode area of 89.6 cm^2. The test rig was housed in a muffle furnace kept at 950 °C, modified to enable fuel and air to be fed to the test module, and to allow electrical measurements to be made. The *I–V* tests were performed at atmospheric pressure with different fuel flows of $H_2/H_2O/CO/CO_2$ mixtures and with air used as the oxidant.

3. Theoretical model

A simulation model has been set up, whose results have been compared to the experimental results obtained as described in the previous section. The model includes the calculation of the local electrochemical kinetics of the IP-SOFC reactor, coupled to the mass balances of the gaseous flows. Since all the experimental data are collected from IP-SOFC modules kept within an oven at high temperature, where radiation is a very efficient heat exchange process, temperature is considered to be approximately uniform; indeed, even if in some cases temperature gradients can be very serious in SOFCs, the possibility of isothermal behaviour of SOFCs has already been reported in the literature [5]. Thus, the IP-SOFC reactor is considered isothermal in all the calculations, and the energy balances are not included in the current version of the simulation model (details about energy balances for SOFC reactors can be found in the seminal papers about the first SOFC [6] and planar SOFC [7] models). The present model is based upon the following assumptions: (i) one-dimensional model along the *x*-co-ordinate; (ii) uniform distribution of the anodic flow rate among the inner channels of the module; (iii) all the gases flow in the *x* direction, with no transversal flows in the *y* or *z* directions; (iv) all the cells of the module supply the same electrical current; (v) mass balances are written in the plug-flow form along the *x*-co-ordinate [5]; (vi) air is considered as the cathodic reactant and a mixture of $H_2/H_2O/CO/CO_2$ is considered as the anodic one; (vii) shifting reaction is assumed at the equilibrium in the anodic compartment; (viii) the electrochemical oxidation of H_2 is the only electrochemical reaction occurring at the anodic side.

The scheme of the electrochemical reactions is as follows:

$$\tfrac{1}{2}\,O_2 + 2e^- \rightarrow O^{2-} \qquad \text{cathodic reaction}$$

$$H_2 + O^{2-} \rightarrow H_2O + 2e^- \qquad \text{anodic reaction}$$

$$H_2 + \tfrac{1}{2}\,O_2 \rightarrow H_2O \qquad \text{over-all reaction}$$

The number of electrons exchanged is $n_e = 2$.

3.1. Local electrochemical kinetics

In fuel cells, the local rate of the electrochemical reaction is directly proportional to the local electrical current. Thus, the evaluation of the local kinetics is made following a procedure which is rather different than with typical chemical reactors, and is based on the estimate of the local electrical current. To this end, an electrochemical model has been developed, which is based on the evaluation of the local thermodynamic reversible potential (Nernst potential):

$$V_{\text{Nernst}} = \frac{-\Delta G}{n_e F} = \frac{-\Delta G^0}{n_e F} - \frac{R_g T}{n_e F} \ln\left[\prod_i (p_i^0)^{\nu_i}\right] \qquad (1)$$

where p_i^0 are the partial pressure of reactants and products in the bulk anodic and cathodic flows, R_g the universal gas constant, T the operating temperature and F the Faraday's constant. For SOFCs, the open circuit potential (i.e. the potential when no electrical current is flowing through the fuel cell) is usually very close to the Nernst potential, indicating that reversibility is obtained (which is not the case for other types of fuel cells, for example, PEMFCs). Then, when current flows, irreversibilities arise and the operating voltage decreases due to the losses associated with the irreversibilities of the process:

$$V = V_{\text{Nernst}} - \eta \qquad (2)$$

where η includes ohmic, activation and concentration losses:

$$\eta = \eta_{\text{ohm}} + \eta_{\text{act}} + \eta_{\text{conc}} \qquad (3)$$

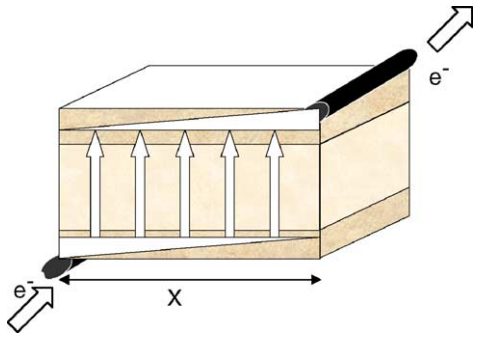

Fig. 2. Path of electrical charges within a single cell.

3.1.1. Ohmic loss

Ohmic losses arise due to the resistances encountered by the electrical charges in their paths internally to the cell. The calculation of the ohmic resistance is based on the evaluation of the resistivity of the materials involved (interconnector, anode, cathode, electrolyte), which is usually temperature dependent [8]:

$$\sigma = \rho^{-1} = \beta_1 \exp\left(-\frac{\beta_2}{T_s}\right) \tag{4}$$

The calculation of the cell/module resistance as a function of the material resistivities accounts for the particular charge paths, which are schematised in Fig. 2. The figure shows the charge paths, which involve in-plane conduction in the electrodes and cross-plane conduction through the electrolyte; both the anodic and cathodic electrodes are covered by their respective porous current collector, which is just an additional superimposed layer (not shown in Figs. 1 and 2). The electrical resistance of this configuration (PEN strip with diagonal terminals) has been evaluated by solving the Ohm's laws applied to the structure, obtaining a result similar to the that reported in [8]:

$$R = CJ\{\coth(J) + B[J - 2\tanh(\tfrac{1}{2}J)]\} \tag{5}$$

where C represents the cross-plane resistance area, E the ohmic symmetry factor, and L the characteristic length:

$$C = \rho_c t_c + \rho_{ccc} t_{ccc} + \rho_{el} t_{el} + \rho_a t_a + \rho_{cca} t_{cca} \tag{6}$$

$$E = \left(\frac{t_{cca}}{\rho_{cca}} + \frac{t_a}{\rho_a}\right)^{-1} \left(\frac{t_{ccc}}{\rho_{ccc}} + \frac{t_c}{\rho_c}\right) \tag{7}$$

$$L = \sqrt{\frac{\rho_{el} t_{el}}{((t_{cca}/\rho_{cca}) + (t_a/\rho_a))^{-1} + ((t_{ccc}/\rho_{ccc}) + (t_c/\rho_c))^{-1}}} \tag{8}$$

$$B = \frac{E}{(1+E)^2} \tag{9}$$

$$J = \frac{X}{L} \tag{10}$$

Finally, the cell ohmic loss is

$$\eta_{ohm} = Ri \tag{11}$$

3.1.2. Activation loss

Activation polarisation is related to the irreversibilities intrinsic in the electrochemical reaction. The activation polarisations η_{act} are expressed in implicit form by the Butler–Volmer equation:

$$i = i_0 \left[\exp\left(\alpha \frac{n_e F}{R_g T}\eta_{act}\right) - \exp\left(-(1-\alpha)\frac{n_e F}{R_g T}\eta_{act}\right)\right] \tag{12}$$

where i_0 is the exchange current density and α the apparent charge transfer-coefficient. Eq. (12) applies to both the anode and the cathode; under open circuit conditions, a direct and reverse electrochemical reactions occur simultaneously at each electrode, both equal to the exchange current density i_0, which can be expressed as a function of the Arrhenius law and of the composition of the reacting gases [5]:

$$i_{0,c} = \gamma_c \left(\frac{p_{O_2}}{p_{ref}}\right)^{0.25} \exp\left(-\frac{E_{act,c}}{R_g T}\right) \tag{13}$$

$$i_{0,a} = \gamma_a \left(\frac{p_{H_2}}{p_{ref}}\right)\left(\frac{p_{H_2O}}{p_{ref}}\right) \exp\left(-\frac{E_{act,a}}{R_g T}\right) \tag{14}$$

3.1.3. Concentration loss

In proximity of the reacting sites in the electrodes, the concentration of reactants and products of the electrochemical reaction is different from the concentration in the bulk flow of the gases, and this is related to a phenomenon of mass transport by diffusion. At each electrode, diffusion occurs in two different ways: (i) external diffusion, in the gas channel, in the boundary layer adherent to the electrode, and (ii) within the porous structure of the electrode, to/from the reaction sites which are usually located at the interface between electrode and electrolyte in the case of the cathode (LSM electrode), or randomly within the electrode in the case of the anode (Ni/YSZ electrode). As a consequence of this effect, the 'true' theoretical reversible voltage of the cell must be calculated through an equation analogous to Eq. (1), but taking into account the reactant/product concentration occurring in proximity of the reaction sites:

$$V_{Nernst} = \frac{-\Delta G}{n_e F} = \frac{-\Delta G^0}{n_e F} - \frac{R_g T}{n_e F} \ln\left[\prod_i (p_i^*)^{\nu_i}\right] \tag{15}$$

where p_i^* denotes the reactant and product partial pressure at the reaction sites. Thus, the difference between Eqs. (1) and (15) gives the departure from the theoretical thermodynamic voltage occurring due to diffusion effect, i.e. the concentration loss:

$$\eta_{conc} = -\frac{R_g T}{n_e F} \ln\left(\frac{p^*_{H_2} p^O_{H_2O}}{p^O_{H_2} p^*_{H_2O}}\right) - \frac{R_g T}{n_e F} \ln\left(\frac{p^*_{O_2}}{p^O_{O_2}}\right)^{1/2} \tag{16}$$

or, expressed in terms of the molar fraction of the gases y_i:

$$\eta_{conc} = -\frac{R_g T}{n_e F} \ln\left(\frac{y^*_{H_2} y^O_{H_2O}}{y^O_{H_2} y^*_{H_2O}}\right) - \frac{R_g T}{n_e F} \ln\left(\frac{y^*_{O_2}}{y^O_{O_2}}\right)^{1/2} \tag{17}$$

where the first term of Eq. (17) represents the anodic concentration overpotential while the second term the cathodic one. Following a treatment analogous to that of [9], it can be shown that, by (i) neglecting the external diffusion; (ii) considering the electrochemical reaction occurring only at the interface between the electrode and the electrolyte; (iii) applying the treatment of diffusion over a stagnant film; (iv) relating the diffusive flows of hydrogen, oxygen and water to the electrical current density i through the Faraday's law, and (v) assimilating multicomponent diffusion to binary diffusion, where necessary; then the molar fractions of oxygen, hydrogen and water at the reaction sites can be calculated from the following equations:

$$y^*_{O_2} = 1 + (y^0_{O_2} - 1)\exp\left(\frac{iR_gTt_c}{4n_eFD_{eff,c}P}\right) \quad (18)$$

$$y^*_{H_2} = y^0_{H_2} - \frac{iR_gTt_a}{2n_eFD_{eff,a}P} \quad (19)$$

$$y^*_{H_2O} = y^0_{H_2O} + \frac{iR_gTt_a}{2n_eFD_{eff,a}P} \quad (20)$$

In the equations, t_c and t_a represent the thickness of the cathode and anode, respectively; P the total pressure, and D_{eff} the effective diffusion coefficient either at the anode or cathode. To evaluate the effective diffusion coefficient the Bosanquet formula [10] has been used:

$$\frac{1}{D_{eff}} = \frac{1}{D_{12}} + \frac{1}{D_{1k}} \quad (21)$$

where the diffusion coefficient for binary mixtures D_{12} is estimated by the equation proposed by Hirschfelder, Bird and Spotz [11], and the Knudsen diffusion coefficient for species 1 is given by free molecule flow theory [10]. Finally, combining Eqs. (17)–(20) the anodic and the cathodic concentration overvoltages are given by

$$\eta_{conc,a} = -\frac{R_gT}{n_eF}\ln\left(\frac{1 - (iR_gTt_a/n_eFD_{eff,a}Py^0_{H_2})}{1 + (iR_gTt_a/n_eFD_{eff,a}Py^0_{H_2O})}\right) \quad (22)$$

$$\eta_{conc,c} = -\frac{R_gT}{2n_eF}\ln\left(\frac{1}{y^0_{O_2}} - \left(\frac{1}{y^0_{O_2}} - 1\right) \times \exp\left(\frac{iR_gTt_c}{2n_eFD_{eff,c}P}\right)\right) \quad (23)$$

Concentration overpotentials can be very high in low temperature fuel cells, where they often cause the occurrence of limiting currents (such as in PEMFCs, which operate at 80 °C). However, they are less critical in SOFCs, due to the high operating temperatures (about 1000 °C).

3.2. Mass balances

The mass balances read as follows:

$$\frac{dW_i}{dx} = r_i \quad (24)$$

Table 1
Model parameters and material properties

Parameter	Value
γ_a	5.5×10^8 A/m^2
γ_c	7×10^8 A/m^2
$E_{act,a}$	100×10^3 J/mol
$E_{act,c}$	120×10^3 J/mol
θ_a	0.5
θ_c	0.3
$\beta_{1,a}$, $\beta_{2,a}$	7800 Ω^{-1} m^{-1}, 1290 K
$\beta_{1,el}$, $\beta_{2,el}$	20500 Ω^{-1} m^{-1}, 9030 K
$\beta_{1,ccc}$, $\beta_{2,ccc}$	33770 Ω^{-1} m^{-1}, 1130 K
σ_{cca}	2×10^{-4} Ω m
σ_c	7.8×10^{-5} Ω m
p_{ref}	1.0133×10^5 Pa
D^{eff}_a, D^{eff}_{cca} (at 1000 °C)	2.1×10^{-5} m^2 s^{-1}
D^{eff}_c, D^{eff}_{ccc} (at 1000 °C)	5.4×10^{-6} m^2 s^{-1}

where the subscript i denotes the reacting species (H_2, O_2, H_2O, CO and CO_2), W the molar flow rate and r the reaction rate, which is related to the electrical current density I (according to the Faraday's law):

$$r_{H_2O} = \frac{i}{b_an_eF} - r^{shift} \quad (25)$$

$$r_{H_2} = -\frac{i}{b_an_eF} + r^{shift} \quad (26)$$

$$r_{O_2} = -\frac{i}{2b_cn_eF} \quad (27)$$

$$r_{CO} = -r^{shift} \quad (28)$$

$$r_{CO_2} = r^{shift} \quad (29)$$

where b is the thickness of the duct where the gases flow. The scheme above includes also Eqs. (28) and (29), which relate the reaction rate of CO and CO_2 to the shifting reaction rate r^{shift}. The shifting reaction is at equilibrium (hypothesis vii); the equilibrium constant is the same over the different cells of the modules, but compositions change, due to the continuous subtraction of hydrogen and production of water related to the electrochemical reaction; the reaction rate r^{shift} is evaluated on this basis.

3.3. Model parameters and material properties

The values of model parameters and material properties used to run the model are reported in Table 1. Most of the values have been taken from the literature [8], or derived as described in Section 4.1.

4. Model results and validation

4.1. 3-Cell results

At first, the simulation results obtained for the 3-cell module are presented and compared to the experimental data. All

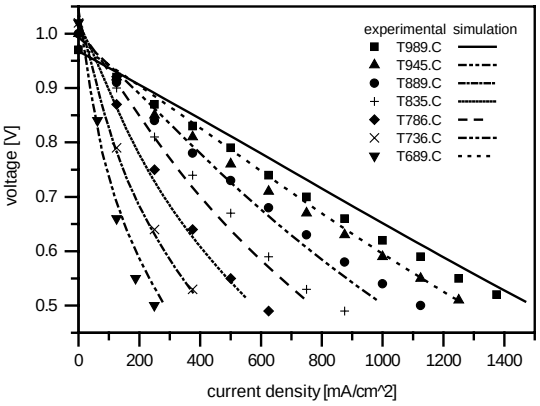

Fig. 3. Comparison between simulation and experimental results for the 3-cell module fed with H_2/H_2O at the anode and air at the cathode.

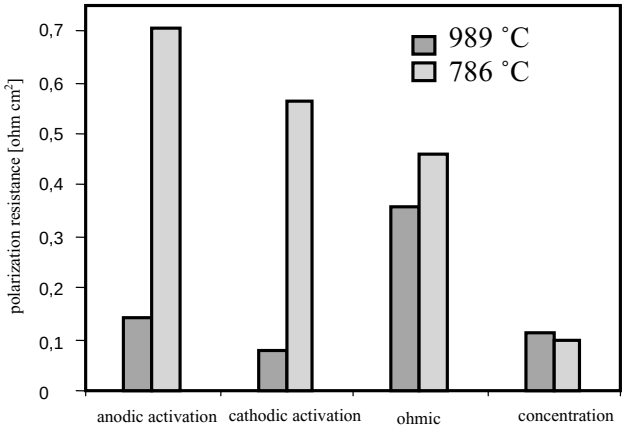

Fig. 4. Relative importance of the various sources of overpotential at different temperatures (simulation results).

the experimental data have been obtained by keeping the cell in a furnace at uniform and controlled temperature, and thus the simulations have been run by keeping the temperature of the solid uniform and equal to the experimental values. The experimental reactant flow rates were very high, and thus the consumption of the reactants was very low, leading to almost uniform gas compositions all over the module. In particular, a value of 6 N l/min has been assumed as the feeding flow rate at the anodic side (97% H_2, 3% H_2O), and 14 N l/min at the cathodic side. Under these conditions, the experimental data are useful in order to calibrate and validate the electrochemical part of the model. Fig. 3 shows the results obtained in terms of characteristic current–voltage curves. The voltage reported in the ordinate is the average among the voltages of the three cells (which, anyway, are very close to each other), while the current density reported in the abscissa, is exactly the same for each of the three cells, since the cells are electrically connected in series. To generate the set of curves in the figure, the less-known parameters (coefficients γ and E_{act} in Eqs. (13) and (14)) were treated as adjustable parameters, and were chosen in the range indicated by previous literatures results; the model was calibrated to the 950 °C data (Table 1) and then only the temperature was changed to generate the curves for the rest of the operational temperatures. Since the electrochemical model is extremely sensitive to temperature, the good agreement between simulation and experimental data obtained in a wide temperature range (from 689 to 989 °C) allows us to assume that the equations and the coefficients used to set the model are physically correct. The average error is about 2.5%, which is of the same order of magnitude, or even lower, than the experimental error of the thermocouples used to measure the operating temperature for every set of experimental data. The analysis of Fig. 3 leads to some considerations: (i) the open circuit potential increases for decreasing operating temperature. Indeed, this is a widely known result for SOFCs, which is due to the fact that for SOFCs (unlike other fuel cells, like PEMFCs) the open circuit potential is in good agreement with the thermodynamic reversible potential (Eq. (1)), which in turn is directly proportional to the ΔG of the electrochemical reaction, which decreases with increasing temperature; (ii) the slope of the characteristic curves increases with decreasing temperature, which is related to the increase of both ohmic and activation effects; and (iii) the characteristic curves are not perfectly straight lines and this becomes more pronounced at low temperatures. In order to explain this effect, we must consider that the relative importance of the different source of overpotentials is different at different operating temperatures. The model results reported in Fig. 4 show that concentration polarisations can be considered of minor importance at all temperatures in the case study, and this is due to (i) the high level of porosity of the materials, (ii) the high diffusion coefficient at the SOFC operating temperatures, and (iii) the high bulk concentration of both anodic and cathodic reactants. In addition to concentration losses, also ohmic and activation polarisations occur, and Fig. 4 shows that at high temperature ohmic overpotentials are the prevailing source of loss (being about twice as large as the sum of anodic and cathodic activation overpotentials), while at low temperatures activation overpotentials are the prevailing contribution. While ohmic losses are a linear function of the electrical current at all temperatures (Eq. (11)), activation overpotentials show different behaviour at different operating temperatures. Indeed, if we take the Butler–Volmer equation (Eq. (12)) into consideration, at high temperatures the term $\alpha F\eta^{act}/R_gT$ is small, and thus easily linearisable, so that the relationship between activation overpotential and electrical current can be considered as linear without considerable errors. On the contrary, at low operating temperatures, linearisation is no longer acceptable. In these conditions, either the first of the second term (depending on whether the cathode or the anode is under study) of the right hand side of Eq. (12) is negligible for almost every operating current (except for extremely small ones [8]), the activation overpotential is a logarithmic function of the electrical current. Thus, at high temperature both ohmic and activation polarisations show a linear *V–I* relationship, and this ex-

plains why both the experimental and theoretical *V–I* curves appear rather linear, while at low temperature, where the activation polarisation is a logarithmic function of current and accounts for the largest part of the overall polarisation, both the experimental and theoretical *I–V* curves show a marked bending.

Another remark is that anodic activation losses are higher than the cathodic ones in the case study. Under other operating conditions (with higher content of water at the anodic side) the anodic activation is usually lower than the cathodic one, but in the present case the anodic activation is rather high due to the fact that, as mentioned before, the water content of the feeding fuel is only 3%; indeed (Eq. (14)), the anodic polarisation tends to be high when the amount of water in the feeding fuel is small.

For a deeper comprehension of the effect of the various parameters on the cell kinetics, the effect of various geometric and chemical–physical parameters has been investigated. Only ohmic and concentration overpotentials have been analysed, since the activation overpotential has a simple analytical expression which depends only on reactant concentration and temperature; furthermore, the effect of the latter parameter has already been analysed in Fig. 4. The cell pitch length *X* (represented in Fig. 2) has a strong effect on the ohmic resistance (Fig. 5a), since, by increasing that parameter, the in-plane path of the electrical charges along the thin electrodes increases; this indicates that small cells would have higher performance (which has also been demonstrated experimentally); nevertheless, it is very difficult to manufacture cells with a pitch smaller than 8 mm. Also the effect of the electrode and electrolyte thicknesses has been investigated. Indeed, an increase of the electrolyte thickness (not reported in Fig. 5) simply causes a significant increase of the internal resistance, since the electrolyte is the material showing the highest resistivity within the cell. On the other hand, Fig. 5b shows that an increase of the electrode thicknesses lowers the overall ohmic resistance; this is due to the fact that an increase of the electrode thickness has the main consequence of increasing the thickness for the passage of the electrical charges during their in-plane path within the electrode, and this is significantly beneficial in decreasing the ohmic losses. However, as a side-effect, an increase of electrode thickness would have a (minor) impact on the concentration polarisations, as demonstrated by Fig. 5c, where the concentration polarisation obtained at 850 °C in an anode fed with a mixture of 3% H_2O/97% H_2 is shown. The results reported in Fig. 5d are obtained under the same operating conditions, with various H_2/H_2O ratios in the fuel feeding, and demonstrate that the concentration overpotentials are higher when either H_2 or H_2O concentration in the

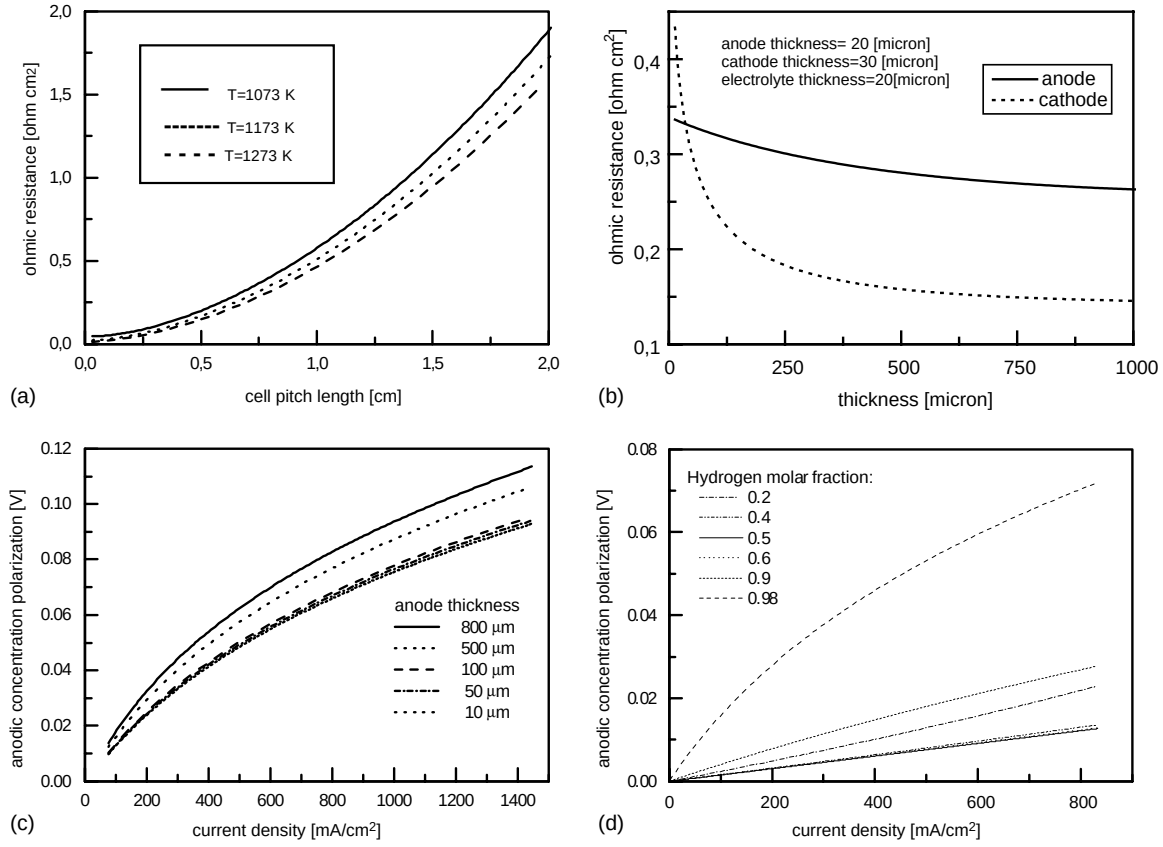

Fig. 5. Influence of various geometric and chemical–physical parameters on ohmic resistance and concentration polarisation. In (d), lines obtained for hydrogen molar fractions of 0.4, 0.5 and 0.6 are almost superimposed to each other.

anodic reactant is low, which can occur in the cells located at the module ends. Fig. 5d also shows that the minimum anodic concentration overpotential is found for $y_{H_2} = 0.5$.

4.2. 20-Cell results

While the 3-cell module has mainly experimental purposes for the evaluation of the performance of materials or cell geometry, the 20-cell module is a prototype of an industrial IP-SOFC unit for commercialisation. In particular, since one of the possible applications of SOFCs is in hybrid systems, whose design is usually made through detailed plant simulation tools, a detailed model of an IP-SOFC module requires experimental validation, in order to guarantee the necessary reliability. Thus, also in this case, a comparison has been made between the experimental and the modelling results. The latter have been obtained by using for the model parameters the same values which have been obtained in the previous section, since all the materials and fabrication techniques are exactly the same with both the 3-cell and the 20-cell modules. However, we must take into account that, since the area of the module is much higher with the latter than with the former experimental unit, there is also a larger chance of having some defects in the structure, and thus a slightly lower experimental performance must be expected. Indeed, solid oxide materials are rather fragile, and thus the presence of some micro-cracks, leading to (i) a not perfect adherence between the different layers which compose each cell, and (ii) to some cross-over of the reactant gases between the anodic and the cathodic sides. Simulation has already pointed out the occurrence of similar effects in other types of SOFCs [5]; in particular, these effects can be taken into account in the simulation by (i) introducing an additional constant resistance, called contact resistance, taking into account the non-perfect contact among the different layers, and (ii) considering that, as a result of leakage, a chemical reaction between oxygen and hydrogen occurs, causing the presence of water in both the anodic and the cathodic flow rates even under open circuit conditions. Indeed, the presence of this additional water at the cathodic side has very little effect on the open circuit potential (Eq. (1)), only related to dilution and the associated decrease of p_{O_2}; on the contrary, it has a strong influence if considered at the anodic side. Thus, the leakage effect has been simulated by considering an additional small flow rate of water only into the inlet anodic stream. In all the results reported in the following, a contact resistance of 0.05 Ω, and a fictitious water flow rate of 0.2 N l/min into the inlet anodic stream has been considered. The simulation results obtained for three different fuel compositions currently under consideration for feeding the modules when included into a whole hybrid system are reported in Fig. 6 (case 1: 100% H_2; case 2: 66.7% H_2, 25.3 % CO, 8% CO_2; case 3: 66.7% H_2, 13.3% CO, 20% CO_2; all the flow rates are humidified at ambient temperature before being fed into the module). It is interesting to observe that different *V–I* curves are obtained under the three cases under consideration: the best performance is obtained in case 1, with pure hydrogen, while, among cases 2 and 3, which are characterised by the same percentage of hydrogen in the fuel but different amounts of CO and CO_2, the best performance is obtained in case 2. Indeed, in case 2 the amount of CO is larger (and the amount of CO_2 smaller) than in case 3, and this, due to the shifting reaction occurring inside the module, leads to the production of an amount of hydrogen higher than in case 3, and thus to a better performance both at open circuit and under load conditions. In all cases the agreement with the experimental data obtained from the experimental facility described in Section 2.2 is good, and this confirms the reliability of the model and in particular the appropriateness of the assumption of equilibrium for the shifting reaction.

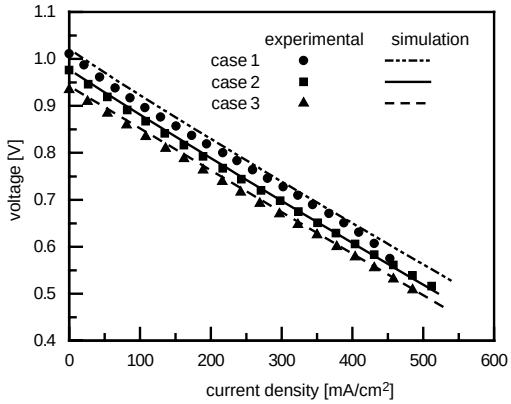

Fig. 6. Comparison between simulation and experimental results for the 20-cell module fed with different $H_2/CO/CO_2/H_2O$ mixtures at the anode and air at the cathode. $T = 950\,^{\circ}C$. Anodic flow rate: 5 N l/min; cathodic (air) flow rate: 6 N l/min.

5. Conclusions

This paper reports satisfactory experimental performance of both a small size and a full-size prototype IP-SOFC module. In both cases the electrical current supplied by the module is above the standard state-of-the-art SOFC performance (0.7 V at a current density of 300 mA/cm^2), which opens interesting application perspectives for this new SOFC concept. A modelling method for simulating the IP-SOFC performance has been presented, whose results have been demonstrated to be in good agreement with the experimental data under a reasonably wide range of operating conditions. Modelling equations and results are discussed in detail, also in view of including the IP-SOFC model into a plant model designed to support simulation and thermodynamic analysis of hybrid IP-SOFC/GT systems.

Acknowledgements

This work is under development within the Framework V EESD project IM-SOFC-GT (EC contract ENK5-CT-2000-

00302). The authors would like to thank Mr. Jim Gardner for his valuable advice on IP-SOFC throughout this work and Mr. Rob Collins at Rolls Royce for running the tests and pre-processing the experimental data.

References

[1] F. Tietz, H.-P. Buchkremer, D. Stöver, Components manufacturing for solid oxide fuel cells, Solid State Ion. 152–153 (2002) 373–381.
[2] N.F. Bessette, W.J. Wepfer, J. Winnic, A mathematical model of a solid oxide fuel cell, J. Electrochem. Soc. 142 (1995) 3792–3800.
[3] S.C. Singhal, Advances in solid oxide fuel cell technology, Solid State Ion. 135 (2000) 305–313.
[4] F.J. Gardner, M.J. Day, N.P. Brandon, M.N. Pashley, M. Cassidy, SOFC technology development at Rolls-Royce, J. Power Sources 86 (2000) 122–129.
[5] P. Costamagna, K. Honegger, Modeling of solid oxide heat exchanger integrated stacks and simulation at high fuel utilization, J. Electrochem. Soc. 145 (1998) 3995–4007.
[6] P.G. Debenedetti, C.G. Vayenas, Steady state analysis of high temperature fuel cells, Chem. Eng. Sci. 38 (1983) 1817–1829.
[7] C.G. Vayenas, P.G. Debenedetti, Y. Yentekakis, L.L. Hegedus, Cross-flow solid-state electrochemical reactors: a steady-state analysis, Ind. Eng. Chem. Fundam. 24 (1985) 316–324.
[8] U.G. Bossel, Facts and Figures, Final Report on SOFC data, IEA report, Operating Task II, Swiss Federal Office of Energy, Berne, CH, 1992.
[9] A. Solheim, K. Nisancioglu, Resistance and current distribution in fuel cell elements, in: Proceedings of the Second International Symposium on SOFC, Athens, Greece, July 1991.
[10] A.F. Mills, Basic Heat and Mass Transfer, IRWIN, Irwin Heat Transfer Series, 1995.
[11] R.B. Bird, W.E. Stewart, E.N. Ligthfoot, Transport Phenomena, Wiley, New York, 1960.